INTERNATIONAL JOURNAL FOR NUMERICAL METHODS IN FLUIDS
Int. J. Numer. Meth. Fluids 2000; **33**: 897–918

Stretched Cartesian grids for solution of the incompressible Navier–Stokes equations

E. J. Avital[a,*], N. D. Sandham[b] and K. H. Luo[a]

[a] *Department of Engineering, Queen Mary & Westfield College, University of London, London, U.K.*
[b] *Department of Aeronautics and Astronautics, University of Southampton, Southampton, U.K.*

SUMMARY

Two Cartesian grid stretching functions are investigated for solving the unsteady incompressible Navier–Stokes equations using the pressure–velocity formulation. The first function is developed for the Fourier method and is a generalization of earlier work. This function concentrates more points at the centre of the computational box while allowing the box to remain finite. The second stretching function is for the second-order central finite difference scheme, which uses a staggered grid in the computational domain. This function is derived to allow a direct discretization of the Laplacian operator in the pressure equation while preserving the consistent behaviour exhibited by the uniform grid scheme. Both functions are analysed for their effects on the matrix of the discretized pressure equation. It is shown that while the second function does not spoil the matrix diagonal dominance, the first one can. Limits to stretching of the first method are derived for the cases of mappings in one and two directions. A limit is also derived for the second function in order to prevent a strong distortion of a sine wave. The performances of the two types of stretching are examined in simulations of periodic co-flowing jets and a time developing boundary layer. Copyright © 2000 John Wiley & Sons, Ltd.

KEY WORDS: incompressible Navier–Stokes equations; Poisson equation; stretching function

1. INTRODUCTION

This study presents two stretching functions of Cartesian grids for solving the unsteady incompressible Navier–Stokes (N–S) equations using the projection method. The incompressibility constraint separates the hydrodynamic field from the acoustic field and thus removes a severe restriction on the time step of the numerical advancement for low Mach number flows. However, the incompressibility constraint also eliminates the time derivative in the continuity equation, leaving an extra constraint that the velocity field should be divergence-free and no obvious way for advancing the pressure field in time. The projection method solves this problem by splitting the time marching into two levels. The first level accounts only for the

* Correspondence to: Department of Engineering, Queen Mary & Westfield College, University of London, Mile End Road, London E1 4NS, U.K.

Received November 1998
Revised May 1999

contributions of the convection and diffusion terms. The second level uses the pressure to project the velocity to a divergence-free space. The pressure is found by solving a Poisson equation.

There are numerous ways to calculate the spatial derivatives appearing in the N–S equations. In this work we consider the Fourier method and the second-order central finite difference scheme, both of which are suitable for Cartesian grids. The Fourier method, implemented by the fast Fourier transform (FFT) technique, has favourable properties when periodic boundary conditions are appropriate. It provides spectral accuracy and a fast solution of the pressure equation. However, the discrete Fourier transform is restricted to the use of an equally spaced co-ordinate. For the most part, this has limited the application of the method to simple flows, such as homogeneous turbulence [1].

Cain *et al.* [2] suggested overcoming the constraint of an equally spaced co-ordinate by using the grid stretching technique. This technique maps an equally spaced co-ordinate in the computational space to a non-equally spaced co-ordinate in the physical space. The spatial derivatives are first calculated in the computational domain using an FFT and then multiplied by the stretching ratio of the mapping to yield the derivatives in the physical space. This should be useful for flows that require high spatial resolution only in a relatively small portion of the stretched co-ordinate, such as shear flows. Cain *et al.* [2] suggested a stretching function that maps the periodic boundaries to infinity in order to eliminate the effect of the boundaries and demonstrated the function on fundamental convection and diffusion problems. This function was later used by Buell [3] to derive an elaborate pseudo-spectral hybrid method, which was used to simulate the early transition of a mixing layer. The first aim of this study is to generalize this stretching function to a class of problem that requires the periodic boundaries at a finite location in the physical domain. It will be shown that this can have the benefit of retaining the diagonal dominance of the matrix of the discretized pressure equation, which is lost if the periodic boundaries are mapped to infinity.

The second-order central finite difference scheme is widely used for non-periodic directions. The scheme demonstrates a consistent behaviour when implemented on a uniform staggered grid. This means no *ad hoc* assumptions for the boundary conditions of the pressure equation and a velocity field that is exactly divergence free as long as the discretized pressure equation is solved exactly up to the machine round-off errors [4]. Such a scheme was used by Kim and Moin [5] with the convection term marched explicitly using the second-order Adams–Bashford scheme and the diffusion term marched implicitly using the Crank–Nicholson method. Special attention was given to the effect of the implicit marching of the diffusion term on the boundary conditions of the intermediate velocity field. Le and Moin [6] modified this scheme by using a third-order Runge–Kutta method for the time marching, where the diffusion term was marched implicitly for each of the sub-steps of the Runge–Kutta method. They suggested a procedure that solves the pressure equation only for the last sub-step of the Runge–Kutta method and thus reduces the computation time. However, this also resulted in reducing the numerical accuracy in time from third-order to second-order.

Non-uniform Cartesian grids were also used for the second-order central finite difference scheme. Sandham [7] used a non-uniform grid in the transverse direction to simulate a channel flow and then compared the results to those produced by a spectral code. Wang *et al.* [8] used a stretched grid in the transverse direction to simulate the breakdown of a laminar boundary

layer over a flat plate. However, in these studies, the operator $\nabla \cdot \nabla$ had to be discretized in the pressure equation instead of ∇^2, in order to keep the consistent behaviour exhibited by the uniform grid scheme. Effectively it meant that the stretching function was differentiated numerically along with the pressure gradient, which could lead to a reduction in the scheme accuracy. The second aim of this study is to derive a new stretching function, so the operator ∇^2 can be directly discretized, while the consistent behaviour of the uniform grid is retained.

The two new stretching functions are derived in Sections 3 and 4 after an explicit time advancement scheme is discussed in Section 2. The merits of the two stretching functions are examined in Section 5 by simulating free and wall-bounded shear flows. A summary is given in Section 6.

2. THE TIME ADVANCEMENT SCHEME

The non-dimensional governing equations for an incompressible viscous flow are the continuity equation

$$\nabla \cdot \bar{v} = 0 \tag{1}$$

and the momentum equation

$$\frac{\partial \bar{v}}{\partial t} = -\nabla \cdot (\bar{v}\,\bar{v}) + \frac{\nabla^2 \bar{v}}{Re} - \nabla p \tag{2}$$

$\bar{v}$ is the velocity vector and p is the pressure. An additional property of a passive scalar f_{ps} governed by

$$\frac{\partial f_{\mathrm{ps}}}{\partial t} = -\nabla \cdot (f_{\mathrm{ps}} \bar{v}) + \frac{\nabla^2 f_{\mathrm{ps}}}{Re\,Sc} \tag{3}$$

$Sc = 1$, can also be simulated to provide an illustration tool for the flow, to compute mixing characteristics and to provide an indicator of the numerical resolution [9].

The following scheme adapts the principle of the projection method to derive an explicit time advancement scheme using a third-order compact Runge–Kutta method. Rewriting Equation (2) as

$$\frac{\partial \bar{v}}{\partial t} = f(\bar{v}) - \nabla p \tag{4}$$

yields the scheme

$$\tilde{\bar{v}}^{r,s} = \bar{v}^{r-1,1} + a_{rs} f(\bar{v}^{r-1,2}) \Delta t \tag{5}$$

$$\bar{v}^{r,s} = \tilde{\bar{v}}^{r,s} - a_{rs} \Delta t \nabla p^{r,s} \tag{6}$$

where r is the sub-step index of the three-step Runge–Kutta method. There are two velocity fields that are marched in time. These are denoted by the index s. They are identical at time t_n

$$\bar{v}^{0,1} = \bar{v}^{0,2} = \bar{v}\big|_{t=t_n} \tag{7}$$

and also at time $t_n + \Delta t$

$$\bar{v}\big|_{t=t_n+\Delta t} = \bar{v}^{3,1} = \bar{v}^{3,2} \tag{8}$$

The pressure $p^{r,s}$ is found by requiring $\bar{v}^{r,s}$ to be divergence free, yielding, using Equation (6), the Poisson equation

$$a_{rs}\Delta t \nabla^2 p^{r,s} = \nabla \cdot \tilde{\bar{v}}^{r,s} \tag{9}$$

A family of constants a_{rs} for the compact Runge–Kutta method is given by Wray [10], one example being

$$a_{r1} = \left(\frac{1}{4}, \frac{3}{20}, \frac{3}{5}\right), \qquad a_{r2} = \left(\frac{2}{3}, \frac{5}{12}, \frac{3}{5}\right) \tag{10}$$

The time marching of the passive scalar f_{ps} follows the regular pattern of the Runge–Kutta method.

This basic scheme was also considered by Le and Moin [6], who added an implicit time marching for the diffusion term and approximated $p^{r,s}$ ($r \leq 2$) by $p^{3,s}$ of the previous step and a ratio of a_{rs}. So Equation (9) can be solved only once per time step. Here, the implicit time marching of the diffusion term was not implemented because it required solving additional elliptic equations and was found unnecessary for the cases studied in Section 5 in terms of numerical stability and accuracy. The pressure modification of Le and Moin [6] was found to reduce the computation time and thus was implemented in some of the cases in Section 5. However, this modification had no effect on the analysis presented in Sections 3 and 4.

3. A STRETCHING FUNCTION FOR THE FOURIER TRANSFORM

For a scheme that uses the Fourier method, it is convenient to carry out the time advancement in Fourier space. A fast way to calculate the non-linear terms in Equations (2) and (3) is to perform the multiplication in real space and transform the result back to Fourier space. To avoid aliasing errors, which can be significant if the grid is not fully resolved, the multiplication should be zero-padded by an additional 50 per cent modes, see Canuto *et al.* [11] for further details.

In Fourier space, the Poisson equation (9) simply becomes

$$-|\bar{k}|^2 \hat{p} = \hat{f} \tag{11}$$

for a uniform grid, where $\bar{k}$ is the wave vector, $\hat{p}$ is the Fourier transform of $p^{r,s}$ and $\hat{f}$ is of the rest of Equation (9). The solution $\hat{p}$ is unique for every $\bar{k}$, except for $\bar{k}=0$, where $\hat{p}$ is arbitrary since the pressure appears as a derivative the momentum equation (2). Accordingly, $\hat{f}$ of $\bar{k}=0$ has to be zero, which is the compatibility condition. The periodic boundary conditions ensure that this condition is met.

A stretching function for the Fourier method has to be periodic and should avoid introducing new interactions between the modes as much as possible. This is, to avoid aliasing errors and additional complexity of the discretized Poisson equation. Here, a generalized form of Cain *et al.*'s [2] mapping is suggested to allow the option of keeping the periodic boundaries in a finite distance from each other and at the same time concentrate more points at the centre of the box. The mapping is

$$\frac{\mathrm{d}s}{\mathrm{d}y}=\alpha+\beta\,\sin^2(\pi s),\quad 0\le s\le 1 \tag{12}$$

where y is the co-ordinate in physical space and s is the equally spaced co-ordinate. When $\alpha=0$, Equation (12) degenerates to Cain *et al.*'s [2] mapping and the boundaries are mapped to infinity. In this work we consider the case $\alpha,\beta>0$, which avoids singularities in the mapping.

The derivatives with respect to y can be calculated using the chain rule, yielding for the first derivative

$$\frac{\mathrm{d}p}{\mathrm{d}y}=\sum_{-(N_y/2)+1}^{(N_y/2)-1} c_j\,\mathrm{e}^{\mathrm{i}k_j s},\quad c_j=\mathrm{i}(\alpha+\beta/2)k_j\hat{p}_j-\mathrm{i}\beta(k_{j-1}\hat{p}_{j-1}+k_{j+1}\hat{p}_{j+1})/4 \tag{13}$$

and for the second derivative

$$\frac{\mathrm{d}^2p}{\mathrm{d}y^2}=\sum_{-(N_y/2)+1}^{(N_y/2)-1} d_j\,\mathrm{e}^{\mathrm{i}k_j s},\quad d_j=-\sum_{n=-2}^{n=2}(-1)^n k_{j+n}\hat{p}_{j+n}g_{j,n} \tag{14}$$

where

$$g_{j,-2}=\frac{(k_{j-2}+2\pi)\beta^2}{16},\qquad g_{j,-1}=\frac{(k_{j-1}+\pi)(2\alpha\beta+\beta^2)}{4} \tag{15.1}$$

$$g_{j,0}=k_j(\alpha^2+\alpha\beta+3\beta^2/8) \tag{15.2}$$

$$g_{j,1}=\frac{(k_{j+1}-\pi)(2\alpha\beta+\beta^2)}{4},\qquad g_{j,2}=\frac{(k_{j+2}-2\pi)\beta^2}{16} \tag{15.3}$$

N_y is the number of points in the y-direction, $k_j=2\pi j$ and $\hat{p}_j$ is to be taken as zero for $|j|\ge N_y/2$. The truncation errors due to the introduction of the stretching are proportional to $\hat{p}_{(N_y/2)-1}$ and $\hat{p}_{(N_y/2)-2}$. The convection and diffusion terms can be calculated using Equations (13) and (14). This will be examined using a practical test case in Section 5. For the rest of this

section, we follow Cain *et al.* [2] and examine the effect on the pressure solution, which has universal characteristics and can considerably affect the execution time.

First, we assume the mapping is applied only in one direction, say the y-direction, while the other two directions are periodic. Then, instead of solving $(N_x-1)(N_z-1)N_y/2$ scalar equations of (11) for the complex variable $\hat{p}$, one has to solve $(N_x-1)(N_z-1)$ equations of the set

$$b_{jm}\cdot\hat{p}_m=\hat{f}_j, \quad j,m=0,\ldots,(N_y/2)-1 \tag{16}$$

where **b** is a pentadiagonal matrix. Its non-zero coefficients in the rows $j=2$ to $(N_y/2)-1$ are

$$b_{j,j-2}=-k_{j-2}g_{j,-2}, \qquad b_{j,j-1}=k_{j-1}g_{j,-1} \tag{17.1}$$

$$b_{j,j}=-k_x^2-k_z^2-k_jg_{j,0} \tag{17.2}$$

$$b_{j,j+1}=k_{j+1}g_{j,1}, \qquad b_{j,j+2}=-k_{j+2}g_{j,2} \tag{17.3}$$

where any contribution from $k_j>2\pi[(N_y/2)-1]$ is set to zero. Any contribution from $k_j<0$ is to be added using the relation

$$\hat{p}(-k_j)=\text{conjugate}[\hat{p}(k_j)] \tag{18}$$

for real data [2]. Thus, the non-zero coefficients of row $j=0$ are

$$b_{00}=-k_x^2-k_z^2, \qquad b_{01}=k_1g_{0,1}+k_{-1}g_{0,-1}, \qquad b_{02}=-k_2g_{0,2}-k_{-2}g_{0,-2} \tag{19}$$

and of row $j=1$

$$b_{10}=0, \qquad b_{11}=-k_x^2-k_z^2-k_1g_{1,0} \tag{20.1}$$

$$b_{12}=k_2g_{1,1}, \qquad b_{13}=-k_3g_{1,2} \tag{20.2}$$

A sufficient condition for a matrix to be non-singular is to require it to be strictly diagonally dominant [12], which yields for **b**

$$|b_{jj}|>\sum_{m\neq j}|b_{jm}|, \quad j=0,\ldots,(N_y/2)-1 \tag{21}$$

When the grid is uniform, the set of the scalar equations (11) obeys Equation (21), except for the mode $\bar{k}=0$, which by physical grounds should be singular. In the case of the stretched grid, the matrix that is least diagonally dominant is the one with $k_x=k_z=0$. Imposing Equation (21) to this mode, leads to, using Equations (17), (20) and (21)

$$\frac{\alpha}{\beta}>\frac{1+\sqrt{4j^4+8j^2+1}}{4j^2}, \quad j=1,\ldots,(N_y/2)-1 \tag{22}$$

as the condition for diagonal dominance. The right-hand side of Equation (22) decreases monotonically from 1.151 for $j=1$ to 0.5 for $j\to\infty$. It shows there is a limit to the amount of stretching that can be achieved if the loss of the diagonal dominance is to be avoided. Condition (22) is not valid for $j=0$ and that row is not diagonally dominant for the matrix with $k_x=k_z=0$. However, this matrix should be singular on the same physical grounds as Equation (11) should be in the case of $\bar{k}=0$. Therefore, if the compatibility condition is fulfilled, row $j=0$ can be ignored for $k_x=k_z=0$ by setting a value for $\hat{p}_0$ (Hildebrand [13]) which leads to a non-singular matrix if condition (22) is met.

Condition (22) ensures that all the other rows in the other matrices with $k_x\neq 0$ or $k_z\neq 0$ are diagonally dominant except for the row that corresponds to $j=0$. Requiring this row to be diagonally dominant imposes an upper limit on the box length in the uniform directions in the form of

$$\frac{2}{L_{x_i}^2} > \beta(\alpha+\beta) \tag{23}$$

where L_{x_i} is that length.

The analysis for the case in which two directions are mapped is given in Appendix A. It results in a much wider band of non-zero coefficients in **b** and more restrictions on the stretching imposed by the condition of diagonal dominance. A similar analysis can be carried out for the case where all three directions are mapped. This should result in an even wider band of non-zero coefficients in **b** and more restrictions imposed by the diagonal dominance condition. The rare need for such a case kept us away from that analysis and instead it was preferred to concentrate on the non-periodic case, which is discussed in the next section.

In practice, it is sometimes difficult to comply with all the restrictions that are imposed by the diagonal dominance on the stretching. Violating these restrictions does not necessarily mean that **b** becomes singular. However, it means that iterative methods for solving the Poisson equation may converge more slowly, if at all. It can also increase the risk of **b** being ill posed, i.e. its determinant may become dangerously close to zero. This can even cause problems to direct solution schemes owing to an increase in the sensitivity to round-off errors. The experience gained in using the iterative bi-conjugate gradient method [14], when one or two directions are stretched, shows that the solution converges rapidly in a few iterations if all the restrictions of the diagonal dominance are met. However, as the ratio of α/β is decreased and more rows lose their diagonal dominance, the convergence rate slows down, especially when α becomes smaller than β, until finally for $\alpha\ll\beta$, the convergence rate becomes too slow to be practical.

4. A STRETCHING FUNCTION FOR THE SECOND-ORDER CENTRAL FINITE DIFFERENCE SCHEME

The periodicity assumption in Section 3 saved the need to consider a boundary condition for the Poisson equation. This is not usually the case for a non-periodic direction. The numerical boundary condition (b.c.) can be derived from Equation (6) as

$$\nabla p_{\Gamma}^{r,s} \cdot \bar{N} = -\frac{(\bar{v}_{\Gamma}^{r,s} - \tilde{\bar{v}}_{\Gamma}^{r,s}) \cdot \bar{N}}{a_{rs}\Delta t} \tag{24}$$

where $\bar{N}$ is a unit vector normal to the boundary Γ (Peyret and Taylor [4]). The problem in Equation (24) is that only $\bar{v}_{\Gamma}^{r,s}$ is known from the physical boundary conditions. However, it can be shown that the value of $\tilde{\bar{v}}_{\Gamma}^{r,s}$ does not affect the calculations for the second-order central finite difference scheme implemented on a staggered uniform grid as in Figure 1. This applies as long as the marching from $\bar{v}^{r-1,s}$ to $\tilde{\bar{v}}^{r,s}$ is explicit, and in that case, $\tilde{\bar{v}}_{\Gamma}^{r,s}$ is usually taken as $\bar{v}_{\Gamma}^{r,s}$. As outlined in Section 1, the goal is to develop a mapping that (i) keeps this property for the b.c. and (ii) the consistent behaviour of an exactly divergence-free velocity field while directly discretizing the Laplacian operator of the pressure equation. The first property is considered in Appendix B. The more elaborate analysis of the second property is discussed next.

To have the velocity exactly divergence-free after the pressure correction, the finite difference scheme has to satisfy the identity

$$\left.\frac{\bar{\mathrm{d}}^2 p}{\bar{\mathrm{d}}x^2}\right|_{i+1/2} = \left.\frac{\bar{\mathrm{d}}}{\bar{\mathrm{d}}x}\left(\frac{\bar{\mathrm{d}}p}{\bar{\mathrm{d}}x}\right)\right|_{i+1/2} \tag{25}$$

where $\bar{\mathrm{d}}/\bar{\mathrm{d}}x$ is the differentiation by the finite difference scheme. For a non-uniform grid one can use the chain role to express the left-hand side of Equation (25) as

$$\left.\frac{\bar{\mathrm{d}}^2 p}{\bar{\mathrm{d}}x^2}\right|_{i+1/2} = \frac{1}{X'^2_{i+1/2}}\left(\left.\frac{\bar{\mathrm{d}}^2 p}{\bar{\mathrm{d}}s^2}\right|_{i+1/2} - \frac{X''_{i+1/2}}{X'_{i+1/2}}\left.\frac{\bar{\mathrm{d}}p}{\bar{\mathrm{d}}s}\right|_{i+1/2}\right) \tag{26}$$

$X(s)$ is the mapping from the equally spaced staggered co-ordinate s to the non-equally spaced co-ordinate x, X' stands for $\mathrm{d}x/\mathrm{d}s$ and X'' for $\mathrm{d}^2x/\mathrm{d}s^2$. Then by using the second-order central finite difference scheme for the differentiation in the s-direction, one gets from Equation (26)

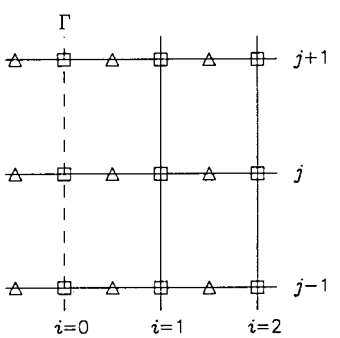

Figure 1. Schematic description of a rectangular grid that is staggered in the streamwise direction. The squares denote where the streamwise velocity is defined and the triangles denote where the pressure is defined. The transverse velocity is defined at the pressure points inside the domain, but its boundary condition is defined at Γ (Peyret and Taylor [4]).

$$\left.\frac{\bar{\mathrm{d}}^2 p}{\bar{\mathrm{d}}x^2}\right|_{i+1/2} = \frac{1}{X'^2_{i+1/2}}\left(\frac{p_{i+3/2} - 2p_{i+1/2} + p_{i-1/2}}{h^2} - \frac{X''_{i+1/2}}{X'_{i+1/2}}\frac{p_{i+3/2} - p_{i-1/2}}{2h}\right) \tag{27}$$

where h is the uniform grid spacing. A similar derivation for the right-hand side of (25) leads to

$$\left.\frac{\bar{\mathrm{d}}}{\bar{\mathrm{d}}x}\left(\frac{\bar{\mathrm{d}}p}{\bar{\mathrm{d}}x}\right)\right|_{i+1/2} = \frac{1}{X'_{i+1/2}h^2}\left(\frac{p_{i+3/2} - p_{i+1/2}}{X'_{i+1}} - \frac{p_{i+1/2} - p_{i-1/2}}{X'_i}\right) \tag{28}$$

A rearrangement of the right-hand side of (28) leads to

$$\begin{aligned}\left.\frac{\bar{\mathrm{d}}}{\bar{\mathrm{d}}x}\left(\frac{\bar{\mathrm{d}}p}{\bar{\mathrm{d}}x}\right)\right|_{i+1/2} = {} & \frac{1}{X'^2_{i+1/2}}\left(\frac{p_{i+3/2} - 2p_{i+1/2} + p_{i-1/2}}{h^2} - \frac{X''_{i+1/2}}{X'_{i+1/2}}\frac{p_{i+3/2} - p_{i-1/2}}{2h}\right) \\ & + Ap_{i+3/2} - (A+B)p_{i+1/2} + Bp_{i-1/2}\end{aligned} \tag{29}$$

where

$$A = \frac{1}{X'_{i+1/2}h^2}\left(\frac{1}{X'_{i+1}} - \frac{1}{X'_{i+1/2}} + \frac{hX''_{i+1/2}}{2X'^2_{i+1/2}}\right) \tag{30.1}$$

$$B = \frac{1}{X'_{i+1/2}h^2}\left(\frac{1}{X'_i} - \frac{1}{X'_{i+1/2}} - \frac{hX''_{i+1/2}}{2X'^2_{i+1/2}}\right) \tag{30.2}$$

In order for Equation (25) to hold, Equation (29) must be identical to Equation (27). This yields two differential finite difference equations in the form of

$$A = 0, \qquad B = 0 \tag{31}$$

These two equations can be initially solved by assuming that the grid is fine enough to allow a slow variation of $X(s)$. Then, one can expand X'_{i+1} around $X'_{i+1/2}$ as

$$X'_{i+1} = X'_{i+1/2} + \frac{h}{2}X''_{i+1/2} + \frac{h^2}{8}X'''_{i+1/2} + \cdots \tag{32}$$

and similarly for X'_i. These expansions can be substituted into Equations (30) and by keeping only the non-zero leading order of h, one just gets one differential equation

$$(X'')^2 - X'X'''/2 = 0 \tag{33}$$

where the index i was omitted because Equation (31) should hold for any i. Equation (33) is in a non-linear form that lacks an explicit dependence on s and hence, according to Hildebrand [15], the solution can be derived as

$$X' = \frac{c_0}{1 + c_1 s}, \quad \text{i.e. } X(s) = \frac{c_0}{c_1} \log(1 + c_1 s) \tag{34}$$

The derivation of (33) from (31) was based on the assumption of a weak variation of $X(s)$ along s. However, substituting (34) into (30) shows that it fulfils (31) *even in the finite difference form*. Satisfying the identity $\bar{\mathrm{d}}^2 p/\bar{\mathrm{d}}x^2 = \bar{\mathrm{d}}(\bar{\mathrm{d}}p/\bar{\mathrm{d}}x)/\bar{\mathrm{d}}x$ also means that (34) allows a free choice of the boundary value $\tilde{\tilde{v}}_1^{r,s}$. A rigorous proof for this is given in Appendix B. Therefore, mapping (34) has met the goals set for it and is unique in doing so because it is the only solution of (33). This should not be a surprise, since $\bar{\mathrm{d}}(\bar{\mathrm{d}}p/\bar{\mathrm{d}}x)/\bar{\mathrm{d}}x$ differentiates numerically $1/X'$ along with $\bar{\mathrm{d}}p/\bar{\mathrm{d}}x$. Thus, if the numerical differentiation is to be kept exact for a second-order polynomial of s, $1/X'$ has to be at the most a linear function of s. On the other hand, consider the simple alternative

$$X' = c_0 + c_1 s \tag{35}$$

which by (28) leads to

$$\frac{\bar{\mathrm{d}}}{\bar{\mathrm{d}}x}\left(\frac{\bar{\mathrm{d}}p}{\bar{\mathrm{d}}x}\right)\bigg|_{i+1/2} = \underbrace{\left[\frac{\mathrm{d}^2 p}{\mathrm{d}x^2}\bigg|_{i+1/2} + \frac{h^2}{6X'^2_{i+1/2}}\left(2\frac{\mathrm{d}^4 p}{\mathrm{d}s^4} - \frac{X''}{X'}\frac{\mathrm{d}^3 p}{\mathrm{d}s^3}\right)_{i+1/2} + \cdots\right]}_{\frac{\bar{\mathrm{d}}^2 p}{\bar{\mathrm{d}}x^2}\Big|_{i+1/2}}\left(1 + \frac{X'^2_{i+1/2} h^2}{4X'_{i+1}X'_i}\right) \tag{36}$$

This shows an additional truncation error that does not exist in the case of Equation (34). Contrary to the grid stretching of the periodic case, (34) does not lead to a loss of the diagonal dominance in $\bar{\mathrm{d}}^2 p/\bar{\mathrm{d}}x^2$ as long as X' is positive and finite. This can be easily verified by Equations (25) and (28). However, in this case, there are other good reasons to limit the stretching. Suppose there is a coherent sinuous motion in the physical domain. Then, the truncation error can be estimated by calculating the modified wave number on the stretched grid [16], which is

$$\tilde{k} = -\mathrm{i}\,\mathrm{e}^{-\mathrm{i}kx}\frac{\bar{\mathrm{d}}}{\bar{\mathrm{d}}x}(\mathrm{e}^{\mathrm{i}kx}) \tag{37}$$

This leads, using (34), to

$$\tilde{k} = -\frac{\mathrm{i}}{2c_0 \breve{X}' h}\left[(1 + \breve{X}' c_1 h)^{\mathrm{i}kc_0/c_1} - (1 - \breve{X}' c_1 h)^{\mathrm{i}kc_0/c_1}\right] \tag{38}$$

where $\breve{X}' \equiv X'/X'(0)$ and $0 \le s \le s_{\max}$. Keeping $|\breve{X}' c_1 h| < O(1)$, which is guaranteed if $\breve{X}'/N_x < O(1)$, leads to

$$\tilde{k} = k\left[1 + \frac{(\mathrm{i}kc_0 - c_1)(\mathrm{i}kc_0 - 2c_1)\breve{X}'^2 h^2}{6} + O(h^4)\right] \tag{39}$$

It shows a second-order accuracy, as sought for, but with an amplitude error as well as a phase error owing to the mapping. Naturally, a uniform grid is more suitable when the flow is dominated by a single coherent sinuous wave. Nevertheless, it emphasizes the need to limit the stretching. Other reasons to do so include the grid-size oscillations, which for this type of finite difference scheme are associated with poor resolution or boundary conditions that are too stiff [17]. An aggressive stretching can worsen this phenomenon [18]. It can also considerably reduce the time step for stability. Therefore, it is recommended to keep the ratio $\breve{X}'/N_x$ smaller than 1 as indicated by the modified wave number analysis and which was found satisfactory in the following boundary layer problem.

5. APPLICATION TO TEST PROBLEMS

A three-dimensional code was written for a Cartesian grid using the time marching scheme described in Section 2. One direction was staggered for the use of the second-order central finite difference scheme of Section 4 and the other two directions were taken as periodic to allow the use of the Fourier method. The Poisson equation for the pressure was solved in the Fourier space using a tri-diagonal solver if no stretching was used or when only the non-periodic direction was stretched. In the case when one of the periodic directions was also stretched an iterative bi-conjugate gradient method was used. The time step was taken at least as half of the upper limit given by a numerical instability analysis based on assuming periodic boundary conditions in all directions and a uniform grid with the physical domain smallest spacing [9]. The same time step was used when results of different grids were compared. This is to ensure the differences in the results are due to the spatial accuracy and not the temporal accuracy. The code was validated by comparing its results to analytical solutions of Stokes flows and Taylor–Green's decaying vortices [5].

Two test problems are discussed in this section. The first is periodic co-flowing jets, which demonstrate the mapping for the Fourier method. The second problem is a time developing boundary layer over a flat plate, which is to demonstrate the stretching function for the central finite difference scheme. In both problems the convergence of the results was checked by refining the mesh whether it was uniform or stretched.

The test problems are two-dimensional to allow generating results for various grids in a reasonable computational effort. Three-dimensional results will be discussed in the future. These will include the simulations of transitional jets and boundary layers with an emphasis on calculating the basic sound sources, which requires an exactly divergence-free velocity field [19]. The spanwise direction will be treated using an FFT.

5.1. Periodic co-flowing jets

Periodic co-flowing jets have been the subject of research due to their importance for multiple-jet burners and nozzles [20]. They exhibit the behaviour of isolated jets when the ratio of the distance between the jets and their diameter is large and the behaviour of flow through a grid when the ratio is close to one. The phenomenon can be simulated by simulating a jet subject to transverse periodic boundary conditions. The grid stretching for the Fourier method

should be useful when interest is in the early stages of the jet development. This is done by concentrating more points in the jet shear layer or by providing a convenient control tool for adjusting the transverse length of the computational box.

A typical mean streamwise velocity for an isolated laminar jet is given by Michalke [21]

$$U(y) = 0.5\{1 + \tanh[b_2(Y/y - y/Y)]\}, \quad b_2 = 0.25\,Y/\delta_2 \tag{40}$$

where the centreline velocity is normalized to one. Y is the jet half-width, which is defined as the point where the velocity is half of its centreline value and δ_2 is the momentum thickness.

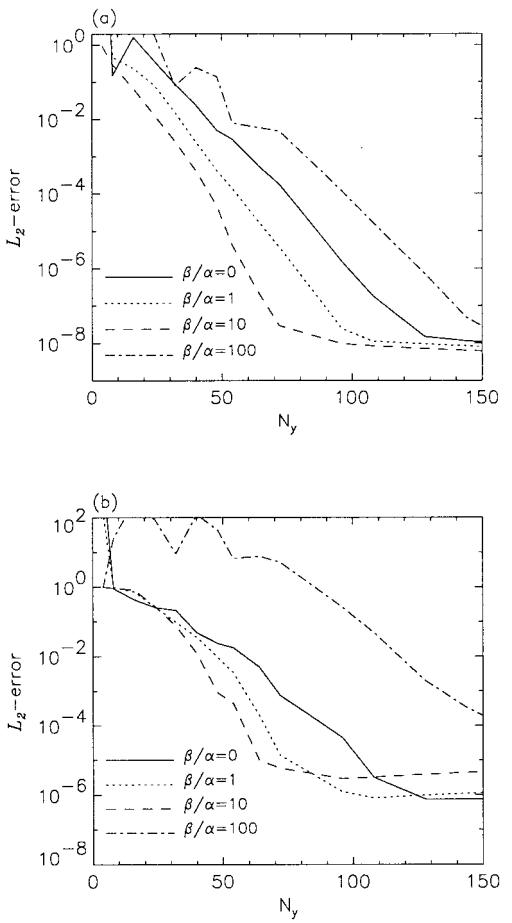

Figure 2. The global L_2-error convergence by the Fourier method for (a) the first derivative and (b) the second derivative of the laminar jet profile (40) and for various grids stretched by (12). The computational box width L_y is five times the jet width $2Y$ and $Y/\delta_2 = 10$.

Figure 2 shows the global L_2-error convergence for the first and second derivatives of $U(y)$, which are calculated by the Fourier method for a uniform and stretched grids. This is to estimate the effect on the convection and diffusion terms. Y/δ_2 was taken as 10 and the velocity profile was confined in the interval

$$-L_y/2 \le y \le L_y/2, \qquad L_y/(2Y) = 5 \tag{41}$$

An exponential convergence typical for a spectral method dominates in the figure until the non-periodicity in the derivatives of $U(y)$ and machine round-off errors come into effect. It is also seen that moderate stretching results in better performance than aggressive stretching. This is because the highest resolution is needed around $y = Y$. Thus, the choice of stretching is not just limited by the desire to keep the diagonal dominance in the discretized Poisson equation but also by the physical nature of the problem.

The simulation of a jet starting with the mean velocity of (40) and confined in the interval of (41) was carried out using the inflow boundary conditions

$$v_x(x = 0, y) = U(y)[1 + \varepsilon \sin(2\pi f t)], \quad v_y = 0 \tag{42}$$

where $\varepsilon = 0.02$ is the disturbance amplitude. The disturbance frequency f was set according to $St_{2Y_0} \equiv 2Y_0 f/U = 0.3$, where $Y_0 = Y(x = 0)$. This is in the range of the jet preferred mode that yields a strong amplification of the disturbance [22]. A soft outflow boundary condition of the form

$$\frac{\partial f}{\partial t} + U_c \frac{\partial f}{\partial x} = 0 \tag{43}$$

was prescribed for the velocity field, where U_c was taken as half of the instantaneous centreline velocity at the outflow [19]. The flow started at $t = 0$ from a parallel state, i.e. $v_x = U(y)$, $v_y = 0$, and was allowed to evolve to a periodic state. The boundary and initial conditions for the passive scalar were taken to be the same as the streamwise velocity, but without the starting disturbance.

Figure 3 shows contour plots of instantaneous vorticity for various grid resolutions and for a computational box with an axial length of $L_x = 20Y_0$. It is seen that a moderate stretching of $\beta/\alpha = 1$ has a similar effect on the vorticity distribution as increasing the transverse resolution from 32 points to 48. However, while the latter caused an increase of more than 50 per cent in the computation time, the stretching caused only a slight increase in the computation time due to the convergence of the pressure solution in a few iterations. Increasing the ratio of β/α to 2 further improved the accuracy of the results in terms of the velocity and passive scalar distributions. However, when β/α was increased to 4 or higher, the trend was opposite and the accuracy deteriorated so much that the simulation had to be stopped. This was clearly caused by the spreading of the jet which led to a need for good resolution further away from the centreline.

The effect of the transverse length of the computational box L_y on the jet development was also investigated. The results are shown in Figure 4 for the streamwise variation of the mean

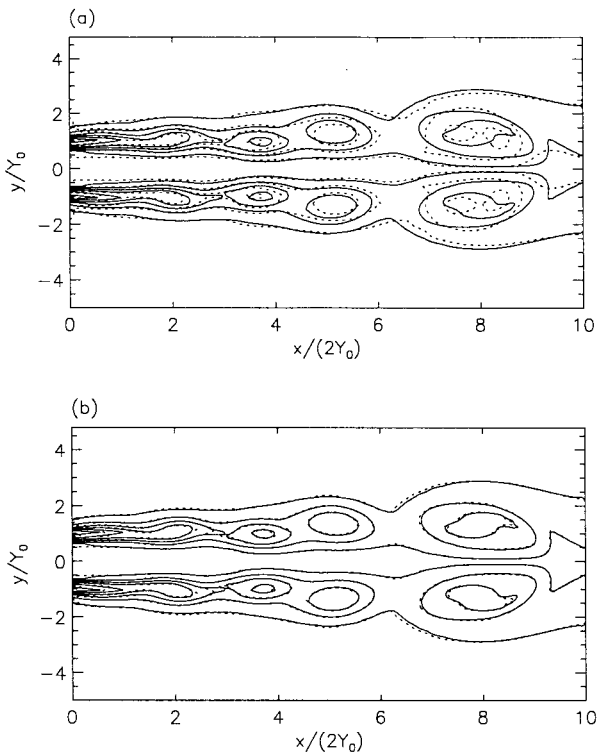

Figure 3. Instantaneous vorticity magnitude contours for a jet subject to transverse periodic boundary conditions and a symmetric inflow disturbance in the streamwise velocity. Re_{2Y_0} is 600 and $Y_0/\delta_2 = 10$. The contour levels range from 0.25 to 4 with an increment of 0.75. The solid lines correspond to a uniform grid with (321, 48) points. The dotted lines correspond to a grid with (321, 32) points, which is (a) uniform and (b) stretched in the transverse direction by (12), where $\beta/\alpha = 1$.

width of the jet. It is seen that the periodicity in the transverse direction can have a strong damping effect on the jet spreading when the computational box width L_y is too close to the jet inflow width $2Y_0$. This phenomenon is usually associated with a self-sustaining instability mechanism dominating the jet development, instead of a convective one as for an isolated jet [20]. Thus, trying to increase the resolution by decreasing L_y can have undesirable effects. The mapping in Section 3 provides a way to avoid these effects without significantly increasing the memory-allocation requirements.

5.2. The time developing boundary layer

The previous problem was dominated by a spatial instability mechanism as long as the transverse length of the computational box was large enough. Thus, this approach is commonly referred to as a spatial simulation. A different approach is to cause deliberately a

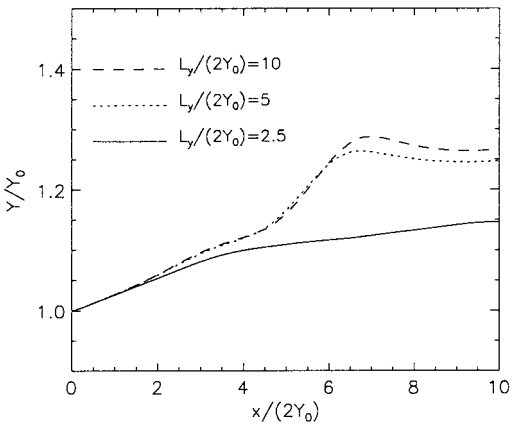

Figure 4. The streamwise variation of the mean width of the jet for various transverse lengths of the computational box. The grid is uniform with (321, 32) points for $L_y = 5Y_0$ and similar resolutions for the other cases of L_y. The rest of the conditions are the same as in Figure 3.

temporal instability mechanism by imposing periodic boundary conditions in the streamwise direction. This approach is usually called a temporal simulation [23]. When it is applied to weakly non-parallel shear flows such as a boundary layer over a flat plate, the hydrodynamic results can be correlated to the results of the spatial simulation by properly replacing the time role in the first approach with the role of the streamwise direction in the latter. The advantage of the temporal approach is that it requires a much smaller box in the streamwise direction than the spatial approach and thus less computational resources.

The time developing boundary layer is a good test case to examine mapping (34), because it requires just the monotonic stretching in one direction that the mapping provides. The simulation was carried out by specifying solid wall boundaries at $x = 0$ and free slip wall boundaries at $x = L_x$, i.e. $\partial v_y/\partial_x = 0$, $v_x = 0$, where x is the non-periodic transverse direction. The flow started from a mean parallel state, i.e. $v_y = v_B$ of a Blasius profile and $v_x = 0$. An initial disturbance was added to the velocity, which corresponds to the most unstable mode of the Orr–Somerfield equation. The disturbance streamwise–velocity amplitude was taken up to 20 per cent of the freestream velocity to accelerate the boundary layer development. The streamwise length of the computational box was taken as the wavelength of the initial disturbance and the transverse length was taken as $10\delta_1$, where δ_1 is the initial mean displacement thickness. The conditions for the passive scalar are the same as for the streamwise velocity but without the initial disturbance.

Figure 5 shows the development of the amplitude of the disturbance mode. It shows that at $t = 0$ a uniform grid of 100 point in the x-direction is sufficient to describe the disturbance accurately. This is not so at $t = 3T$, where $T = 17.2557\delta_1/U$, which is the time period of the initial disturbance calculated by linear stability theory. A gap of about 10 per cent opens up in the mode amplitude between the uniform grid of 100 points to that of 600 points. This is clearly caused by the numerical errors due to the less resolved grid. These errors are

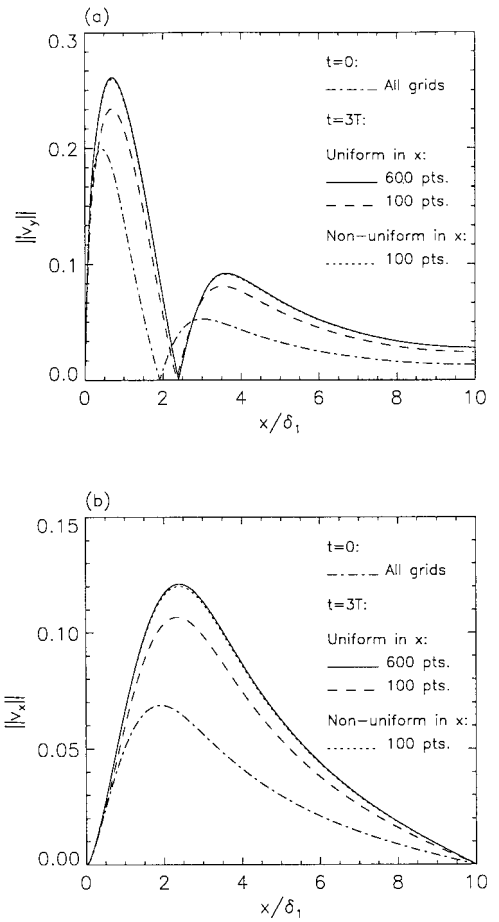

Figure 5. The development of the initial disturbance amplitude of (a) v_y and (b) v_x in the time developing boundary layer case. T is the time period of the initial disturbance calculated by linear stability theory and Re_{δ_1} is 998. The non-uniform grid is stretched by (34) with a maximum factor of $\check{X}'_{\max} = 50$, i.e. $\Delta x_{\max}/\Delta x_{\min} \cong 50$, and having $s_{\max} = x_{\max} = 10\delta_1$.

significantly reduced if mapping (34) is introduced with a maximum stretching factor of $\check{X}'_{\max} = 50$, i.e. $\Delta x_{\max}/\Delta x_{\min}$ is about 50 and where $s_{\max} = x_{\max}$. The relatively coarse mesh also affects the disturbance propagation velocity as seen in Figure 6. This causes a phase shift of about 40° between the relatively coarse uniform mesh and the fine mesh at $t = 3T$.

Figure 7 shows the effects of mappings (34) and (35) on the wall shear $\mathrm{d}v_y/\mathrm{d}x(x = 0)$, which is calculated by the one-sided second order formula

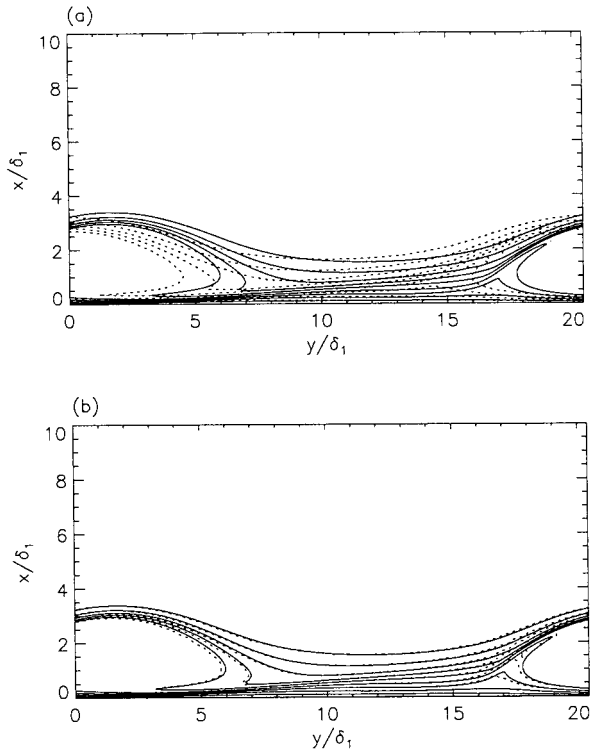

Figure 6. Instantaneous passive scalar contours of the time developing boundary layer of Figure 5 and for $t = 3T$. The contour levels range from 0.1 to 0.9 with an increment of 0.1. The solid lines correspond to a uniform grid with a transverse resolution of 600 points. The dotted lines correspond to a transverse resolution of 100 points, which are (a) equally spaced and (b) are stretched as in Figure 5. The simulations used 32 points in the axial direction.

$$\left.\frac{\mathrm{d}v_y}{\mathrm{d}x}\right|_{x=0} = \frac{-v_y(s=1.5h) + 9v_y(s=0.5h)}{3X'(0)h} \tag{44}$$

where $v_y(s=0)$ is zero due to the wall. To make the comparison between the two mappings as fair as possible, the same $X'(0)$ and h were taken in both mappings. This ensures that only the differences in v_y between the two mappings cause the difference in the wall shear. It also results in about the same $\Delta x_{\min}$, which makes the stability limit for the time step the same and thus results in the same execution time. Figure 7 shows a considereable difference in the wall shear between the fine grid and the coarser uniform grid, i.e. $X'(0) = 1$. This is mostly due to the phase error seen in Figure 6(a). The difference in the wall shear between the fine grid and the coarse grid initially decreases at the same rate for both mappings. However, as the stretching increases the wall shear produced by (34) continues to converge to the fine grid result at almost an exponential rate while the result by (35) shows a reduced rate of convergence.

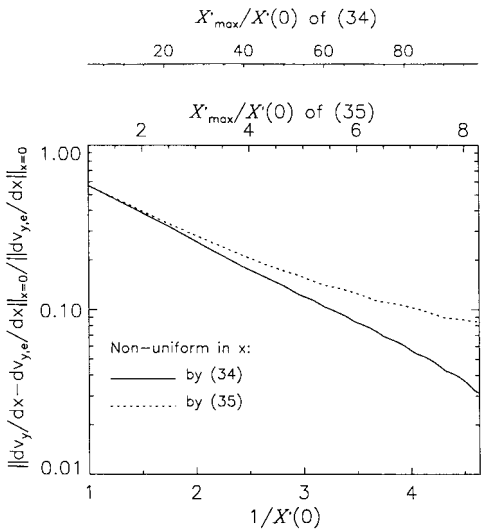

Figure 7. The grid stretching effect on the wall shear of the mode of Figure 5. dv_y/dx is produced by a stretched grid of 100 points in the transverse direction and $dv_{y,e}/dx$ by a uniform grid of 600 points. Both kinds of stretching functions take $s_{\max} = x_{\max}$.

It is difficult to say what is the main cause of the behaviour seen in Figure 7. It can be the better maximum stretching factor $\breve{X}'_{\max}$, i.e. $X'_{\max}/X'(0)$, which is provided by (34). It can also be the higher truncation error in the pressure equation due to (35), which increases as the stretching increases as seen in (36). A similar test for a Stokes problem, where there was no need to solve a pressure equation, showed smaller differences between the two mappings and almost no change in the convergence rate when (35) was used, until that convergence hit its minimum. This leads us to believe that the higher truncation error in the pressure equation due to (35) had something to do with the reduced convergence rate seen in Figure 7. Of course one can try and fit a stretching function to the current problem that may behave even better than (34). However, that function probably will not behave that well when the conditions are changed. The fact that (34) does not introduce an additional truncation error in the pressure equation as other functions do, promises a general good performance as long as there is a physical reason for a monotonic stretching. This was supported by further numerical experimentation that included varying the disturbance amplitude and comparing with linear stability theory results when the amplitude was small enough, say less than 1 per cent.

6. SUMMARY

Two Cartesian grid stretching functions were developed for solving the unsteady incompressible N–S equations using the projection method. The first function is intended for use with the

Fourier method and is a generalization of an earlier version that mapped the periodic boundaries to infinity. The present mapping concentrates more points at the box centre while allowing the box size to remain finite in the physical domain. The mapping keeps the spectral behaviour of the scheme as long as the two highest modes are negligible. The analysis concentrated on the effect of the mapping on the pressure solution while the effect on the convective and diffusion terms was discussed for each of the test cases separately. The diagonal dominance of the pressure equation matrix was shown to be spoiled by the mapping and limits to the stretching were derived for mappings in one direction and two directions.

The second type of stretching was derived to allow a direct discretization of the Laplacian operator in the pressure equation using the second-order central finite difference scheme, while retaining the consistent behaviour of the uniform-grid scheme. This means no *ad hoc* assumptions on the pressure boundary conditions and an exactly divergence-free velocity field after the pressure correction. A unique function was found to fulfil these conditions. It permits a monotonic stretching and does not spoil the diagonal dominance of the pressure equation, as long as it does not stretch to infinity. However, a limit on the stretching was derived in order to prevent strong distortion of a coherent sinuous wave.

The usefulness of the two mappings was illustrated by simulating periodic co-flowing jets and a time developing boundary layer. It was shown that a careful implementation of the stretching functions can achieve a considerable reduction in the required computational resources. Hence, it is suggested that these functions be added to the arsenal of tools available for simulating incompressible flow.

APPENDIX A. STRETCHING TWO PERIODIC DIRECTIONS

Applying mapping (12) in two directions, say y and z, results in a much wider band of non-zero coefficients in **b** than is the case for a single mapped direction. Let us assume that y is the first to be Fourier transformed so that $\hat{p}_m$ can be arranged in a vector form for each k_x, where

$$m = j + (l - l_0)N_y/2, \quad l_0 = -(N_z/2) + 1 \tag{A1.1}$$

$$-N_z/2 + 1 \le l \le (N_z/2) - 1, \quad 0 \le j \le (N_y/2) - 1 \tag{A1.2}$$

This results in having $(N_x - 1)$ equations of the set

$$b_{nm} \cdot \hat{p}_m = \hat{f}_m, \quad 0 \le n, m \le [(N_z/2) - 1](N_y/2) - 1 \tag{A.2}$$

to solve. The non-zero coefficients of **b** at row n are

$$b_{n,n-N_y} = -k_{l-2}g_{l,-2}, \qquad b_{n,n-N_y/2} = k_{l-1}g_{l,-1} \tag{A3.1}$$

$$b_{n,n-2} = -k_{j-2}g_{j,-2}, \qquad b_{n,n-1} = k_{j-1}g_{j,-1} \tag{A3.2}$$

$$b_{n,n} = -k_x^2 - k_j g_{j,0} - k_l g_{l,0} \tag{A3.3}$$

$$b_{n,n+2} = -k_{j+2} g_{j,2}, \qquad b_{n,n+1} = k_{j+1} g_{j,1} \tag{A3.4}$$

$$b_{n,n+N_y} = -k_{l+2} g_{l,2}, \qquad b_{n,n+N_y/2} = k_{l+1} g_{l,1} \tag{A3.5}$$

where the mapping parameters α_z and β_z are to be used in (15) if g has the index l and α_y and β_y for the index j. As of a single mapped co-ordinate, any contribution from $k_j > 2\pi[(N_y/2) - 1]$ or $|k_l| > 2\pi[(N_z/2) - 1]$ is to be set to zero and any contribution from $k_j < 0$ is to be included using (18).

Starting the analysis with the matrix that corresponds to $k_x = 0$, it is found that (22) guarantees that all the rows that do not have $k_j = 0$ or $k_l = 0$ in their diagonal, are diagonally dominant when (22) is imposed on j and l. The row of $k_l = k_j = 0$ in its diagonal has to be subtracted out as in the case of a single mapped co-ordinate. This leaves only the rows that have $k_j = 0$ or $k_l = 0$ in their diagonal vulnerable to a loss of diagonal dominance. Condition (22) shows that as j or l decreases, the diagonal dominance weakens. Hence, imposing diagonal dominance on the rows that have $j = 0$, $l = 1$ in their diagonal or vice versa, guarantees the dominance for all the rest of the rows that possess j or l in their diagonal. This leads, using (A3), to

$$\alpha_z^2 > \alpha_z \beta_z/2 + 3\beta_z^2/4 + \alpha_y \beta_y/2 + \beta_y^2/2 \tag{A4}$$

for $j = 0$, $l = 1$ and vice versa in the indexes y, z for $j = 1$, $l = 0$. If $\alpha_y = \alpha_z$ and $\beta_y = \beta_z$ then (A4) leads to $\alpha/\beta > 1.725$ instead of the $\alpha/\beta > 1.151$ yielded by (22) for the single mapped co-ordinate case.

Complying with all the restrictions outlined for the matrix with $k_x = 0$ also ensures that all the rows of the other matrices are diagonally dominant, except for the rows that have $j = l = 0$ in their diagonal. In that case, one has to impose

$$\frac{2}{L_x^2} > \beta_y(\alpha_y + \beta_y) + \beta_z(\alpha_z + \beta_z) \tag{A5}$$

which is more restrictive when compared with condition (23) of the single mapped co-ordinate case.

APPENDIX B. AVOIDING *AD HOC* ASSUMPTIONS ON THE PRESSURE BOUNDARY CONDITIONS

The goal is to derive the governing equation for the grid stretching that keeps the free choice of the boundary condition $\tilde{\tilde{v}}_\Gamma^{r,s}$ for the second-order central finite difference scheme of Section 4. Assuming an explicit time marching from $\bar{v}^{r-1,s}$ to the intermediate velocity field $\tilde{\tilde{v}}^{r,s}$, the boundary value $\tilde{\tilde{v}}_\Gamma^{r,s}$ can affect only through the pressure solution of the Poisson equation (9) (Peyret and Taylor [4]). Hence, the effect of $\tilde{\tilde{v}}_\Gamma^{r,s}$ must be eliminated from that solution.

A discretization of the Poisson equation (9) at the cell mid-point closest to the boundary Γ yields, using (27) and Figure 1,

$$\left(1+\frac{hX''_{1/2}}{2X'_{1/2}}\right)p_{-1/2}-(2+h^2X'^2_{1/2}\nabla_h^2)p_{1/2}+\left(1-\frac{hX''_{1/2}}{2X'_{1/2}}\right)p_{3/2}=\frac{h^2X'^2_{1/2}}{a\Delta t}\left(\frac{\tilde{u}_1-\tilde{u}_0}{X'_{1/2}h}+\nabla_h\cdot\tilde{\tilde{v}}_{1/2}\right) \tag{B1}$$

where u is the velocity component in the stretched direction and ∇_h is the divergence operator for the other directions. For simplicity, the indices r and s were omitted from (B1). A similar discretization of the boundary condition (24) leads to

$$\frac{p_{1/2}-p_{-1/2}}{X'_0h}=-\frac{u_0-\tilde{u}_0}{a\Delta t} \tag{B2}$$

Equations (B1) and (B2) can be combined to a new equation that does not contain $p_{-1/2}$. The requirement that $\tilde{u}_0$ does not affect the solution means that the coefficient of $\tilde{u}_0$ has to be cancelled out in that equation. This leads to

$$\left(1+\frac{hX''_{1/2}}{2X'_{1/2}}\right)\frac{X'_0}{X'_{1/2}}=1 \tag{B3}$$

which is identical to $B=0$ by (30.2). A similar analysis for the right-hand side boundary leads to the requirement $A=0$ of (31). Thus, mapping (34) found in Section 4 also allows a free choice of the boundary condition $\tilde{\tilde{v}}_\Gamma^{r,s}$ as in the uniform staggered grid.

REFERENCES

1. Moin P, Mahesh K. Direct numerical simulation: a tool in turbulence research. *Annual Reviews in Fluid Mechanics* 1998; **30**: 539–578.
2. Cain AB, Ferziger JH, Reynolds WC. Discrete orthogonal function expansions for non-uniform grids using the fast Fourier transform. *Journal of Computational Physics* 1984; **56**: 272–286.
3. Buell JC. A hybrid numerical method for three-dimensional spatially developing free-shear layers. *Journal of Computational Physics* 1995; **95**: 313–338.
4. Peyret P, Taylor TD. *Computational Methods for Fluid Flow*. Springer: New York, 1983; 143–166.
5. Kim J, Moin P. Application of a fractional-step method to incompressible Navier–Stokes equation. *Journal of Computational Physics* 1985; **58**: 308–322.
6. Le H, Moin P. An improvement of fractional step methods for the incompressible Navier-Stokes equations. *Journal of Computational Physics* 1991; **92**: 369–379.
7. Sandham ND. Resolution requirements for direct numerical simulation of near-wall turbulent flow using finite differences. Report QMW-EP-1097, Department of Aeronautical Engineering, Queen Mary & Westfield College, London, UK, 1994.
8. Wang M, Lele SK, Moin P. Sound radiation during local laminar breakdown in a low-Mach number boundary layer. *Journal of Fluid Mechanics* 1996; **319**: 197–218.
9. Sandham ND, Reynolds WC. A numerical investigation of the compressible mixing layer. Report TF-45, Thermomechanical Division, Department of Mechanical Engineering, Stanford University, 1989.
10. Wray AA. Very low storage time-advancement schemes. Internal Report, NASA-Ames Research Center, Moffet Field, CA, 1986.
11. Canuto C, Hussaini MY, Quarteroni A, Zang TA. *Spectral Methods in Fluid Dynamics*. Springer: Berlin, 1988.
12. Ortega JM. *Numerical Analysis. A Second Course*. SIAM: Philadelphia, PA, 1990; 105–107.

13. Hildebrand FB. *Methods of Applied Mathematics*. Prentice-Hall: Englewood Cliffs, NJ, 1965; 21–23.
14. Press WH, Teukolsky SA, Vetterling WT, Flannery BP. *Numerical Recipes in Fortran*. Cambridge University Press: Cambridge, 1992; 77–82.
15. Hildebrand FB. *Advanced Calculus for Applications*. Prentice-Hall: Englewood Cliffs, NJ, 1963; 38–40.
16. Cain AB, Bush RH. Numerical wave propagation analysis for stretched grids. AIAA Paper No. 94-0172, 1994.
17. Gresho PM, Lee RL. Don't suppress the wiggles—they're telling you something. *Computers and Fluids* 1981; **9**: 223–253.
18. Hahn S, Choi H. Unsteady simulation of jets in a cross flow. *Journal of Computational Physics* 1997; **134**: 342–356.
19. Avital EJ, Sandham ND, Luo KH, Musafir RE. Calculation of basic radiation of axisymmetric jets by direct numerical simulation. *AIAA Journal* 1999; **37**: 161–168.
20. Villermaux E, Hopfinger EJ. Periodically arranged co-flowing jets. *Journal of Fluid Mechanics* 1994; **263**: 63–92.
21. Michalke A. Survey on jet instability theory. *Progress in Aerospace Science* 1984; **21**: 159–199.
22. Crow CC, Champagne FH. Orderly structure in jet turbulence. *Journal of Fluid Mechanics* 1971; **48**: 547–591.
23. Herbert T. Exploring transition by computer. *Applied Numerical Mathematics* 1991; **7**: 3–25.

